nature nanotechnology

SUPPLEMENTARY INFORMATION

DOI: 10.1038/NNANO.2015.32

Inertial Imaging with Nanomechanical Systems

M. Selim Hanay[*], *Scott I. Kelber*[*], *Cathal D. O'Connell*[*], *Paul Mulvaney*, *John E. Sader*[‡], *Michael L. Roukes*[‡]

1. Derivation of Eq. (2) in the main text

Precipitous downward shifts in the modal resonance frequencies of a nanomechanical device occur upon adsorption of individual analytes [1]. These measured frequency shifts can be used to calculate the mass, position, and molecular shape of individual analytes that adsorb upon a NEMS resonator – as described in the main text. Importantly, in the limit where the particle mass is much less than the device mass, the sequential measurement of multiple particles is unaffected by the mass loading due to previous particles.

Previous analyses [1,2] have considered the analyte particles to be point masses. In this work, we model the individual particles as finite-sized objects with a spatial mass distribution that is initially unknown. We consider a general device of arbitrary composition that is loaded by an adsorbate with mass, m, which is much less than the device mass, M. We further assume that the particle size is small compared to the device dimensions (and the wavelengths of the vibrational modes) or, if not, that the particle is much more compliant than the device itself. Under such conditions, which are especially relevant for the case of soft biological molecules (of special interest to us), the vibrational mode shapes of the device are unaffected by the adsorbed analyte, and thus the strain energy of the device is also unchanged. It then follows that the maximum kinetic energy of the device, before and after mass loading, is invariant for the same oscillation amplitude, i.e.,

* *These authors contributed equally to this work.*
‡ Corresponding authors: *jsader@unimelb.edu.au; roukes@caltech.edu*

$$\mathrm{KE}_{\mathrm{unloaded}} = \mathrm{KE}_{\mathrm{loaded}} , \tag{S1}$$

where

$$\mathrm{KE}_{\mathrm{unloaded}} = \frac{1}{2}\left(\omega_n^{(0)}\right)^2 \int_{\Omega} \rho_{\mathrm{device}}(\mathbf{r}) \left|\boldsymbol{\Phi}_n(\mathbf{r})\right|^2 dV , \tag{S2}$$

$$\mathrm{KE}_{\mathrm{loaded}} = \frac{1}{2}\left(\omega_n\right)^2 \int_{\Omega+\Omega_{\mathrm{analyte}}} \left\{\rho_{\mathrm{device}}(\mathbf{r}) + \rho(\mathbf{r})\right\} \left|\boldsymbol{\Phi}_n(\mathbf{r})\right|^2 dV , \tag{S3}$$

where $\rho_{\mathrm{device}}(\mathbf{r})$ is the mass density of the device and $\rho(\mathbf{r})$ is the mass density of the analyte absorbed onto the device surface, $\omega_n^{(0)}$ and ω_n are the angular resonance frequencies of the unloaded and loaded devices, $\boldsymbol{\Phi}_n(\mathbf{r})$ are the natural (vector) vibrational modes of the device in the absence of analyte adsorption, Ω is the spatial integration domain of the device, and $\Omega_{\mathrm{analyte}}$ is the spatial integration domain of the analyte.

We consider an adsorbate that is both thin and compliant with the device surface, *i.e.*, as the device vibrates, the analyte moves with identical velocity to the device surface at any normal position to the surface. This is expected to hold for analytes of sufficiently small mass that the device mode shapes remain unaffected. The volume integral in Eq. (S3) over the analyte's volume can then be replaced by a surface integral involving its areal mass density μ (evaluated by integrating $\rho(\mathbf{r})$ normal to the surface),

$$\int_{\Omega_{\mathrm{analyte}}} \rho \left|\boldsymbol{\Phi}_n\right|^2 dr = \int_{\Omega_s} \mu \left|\boldsymbol{\Phi}_n\right|^2 dS , \tag{S4}$$

where Ω_s is the surface of the device.

Equations (S1) - (S4) then give the following leading-order result

$$\Delta_n \equiv \frac{\omega_n - \omega_n^{(0)}}{\omega_n^{(0)}} = -\frac{1}{2}\frac{\int_{\Omega_s} \mu \left|\mathbf{\Phi}_n\right|^2 dS}{\int_{\Omega} \rho_{\text{device}} \left|\mathbf{\Phi}_n\right|^2 dV} \ , \tag{S5}$$

which is formally valid in the limit of small fractional frequency shifts, Δ_n.

We require that the modes satisfy the normalization condition

$$\int_{\Omega} \rho_{\text{device}}(\mathbf{r}) \left|\mathbf{\Phi}_n(\mathbf{r})\right|^2 dV = M \, , \tag{S6}$$

which, for a device of constant density, coincides with the usual orthonormal condition, *i.e.*, $\int_{\Omega} \left|\mathbf{\Phi}_n(\mathbf{r})\right|^2 dV = 1$. Equations (S4) - (S6) then yield the required result,

$$F_n = -2\,\Delta_n M \ , \tag{S7}$$

where $F_n = \int_{\Omega_s} \rho(\mathbf{r}) \left|\mathbf{\Phi}_n(\mathbf{r})\right|^2 dV$.

2. Evaluating higher moments of the analyte's mass distribution

In the main text, we examined the zeroth moment of the analyte density distribution for a doubly-clamped beam – this gives the analyte mass, m. Since a beam is a one-dimensional device, we derive results for the analyte's linear mass density, $\lambda(x)$, i.e., the mass density integrated over the normal and lateral (*i.e.*, transverse) directions of the beam surface. Here, we extend this analysis to obtain the first three higher-order moments: *(i)* the centre-of-mass of the analyte (position), *(ii)* the analyte's average size (standard deviation), and *(iii)* its skewness (asymmetry).

First moment (position):

To evaluate the position of the analyte, coefficients $\alpha_n^{(1)}$ in Eq. (3) (main text) must be chosen such that

$$g^{(1)}(x)=\sum_{n=1}^{N}\alpha_n^{(1)}\Phi_n^2(x)=x \tag{S8}$$

over the spatial domain, Ω_l, which for a (one-dimensional) beam is $x\in[0,1]$; x is normalized by the beam length, L. Due to the inherent symmetry in $\Phi_n^2(x)$, about $x=1/2$, Eq. (S8) can be applied over either subdomain $x\le 1/2$, or $x\ge 1/2$, but not both. Satisfaction of Eq. (S8) over the subdomain $0\le x\le 1/2$, will thus yield a distribution of $g^{(1)}(x)=1-x$ for $1/2\le x\le 1$. Since the analyte's size is much smaller than the beam length, and the beam is symmetric about $x=1/2$, the choice of subdomain is inconsequential and simply defines the origin.

The particle position is therefore given by:

$$\langle x\rangle\equiv\frac{\int_0^1 x\lambda(x)\,dx}{\int_0^1\lambda(x)\,dx}=\frac{\int_0^1 g^{(1)}(x)\lambda(x)\,dx}{\int_0^1 g^{(0)}(x)\lambda(x)\,dx}=\frac{\mathrm{m}^{(1)}}{\mathrm{m}^{(0)}}=\frac{\sum_{n=1}^{N}\alpha_n^{(1)}\Delta_n}{\sum_{n=1}^{N}\alpha_n^{(0)}\Delta_n}, \tag{S9}$$

This provides the particle position relative to the nearest clamped end of the beam. Note that the particle position is defined by a rational function that involves the fractional-frequency shifts, Δ_n, of N modes. Once these shifts have been experimentally measured, all that is required are the coefficients for the zeroth and first moments, $\alpha_n^{(0)}$ and $\alpha_n^{(1)}$ (see main text).

Since the mode shapes of a doubly-clamped beam have a boundary layer near both clamped ends, whose length scale is $O(1/n)$ relative to the beam length, we choose to evaluate the coefficients $\alpha_n^{(1)}$ over a region that excludes these boundary layers. We select this region to be

$$\frac{N}{1+N^2} \le x \le 1/2 \ , \tag{S10}$$

where $N = 1, 2, 3, \ldots$ represents the highest mode used in the measurement. For the zeroth moment calculated in the main text, which requires $g^{(0)}(x) = 1$, this region is extended to be symmetric about $x = 1/2$.

Evaluating the coefficients $\alpha_n^{(1)}$ using a least-squares fit over the region in Eq. (S10), and using the coefficients $\alpha_n^{(0)}$ determined previously for the zeroth moment (see main text), yields the results in Supplementary Fig. 1a. Note that the function

$$g^{(1)}(x) = \sum_{n=1}^{N} \alpha_n^{(1)} \Phi_n^2(x) \tag{S11}$$

provides an excellent approximation to $g^{(1)}(x) = x$ within the specified measurement zone, Eq. (S10).

Second moment (size):

The size of the analyte is specified by the standard deviation of its density distribution, which requires evaluation of the second moment,

$$g^{(2)}(x) = \sum_{n=1}^{N} \alpha_n^{(2)} \Phi_n^2(x) = x^2 , \tag{S12}$$

over the spatial domain Ω_l. Again the coefficients $\alpha_n^{(2)}$ are obtained using a least-squares analysis over the domain in Eq. (S10) only, due to the small size of the analyte relative to the beam length.

The required variance (square of standard deviation) of the analyte's density is then given by

$$\sigma_x^2 = \frac{\mathrm{m}^{(2)}}{\mathrm{m}^{(0)}} - \left(\frac{\mathrm{m}^{(1)}}{\mathrm{m}^{(0)}}\right)^2 = \frac{\sum_{n=1}^{N} \alpha_n^{(2)} \Delta_n}{\sum_{n=1}^{N} \alpha_n^{(0)} \Delta_n} - \left(\frac{\sum_{n=1}^{N} \alpha_n^{(1)} \Delta_n}{\sum_{n=1}^{N} \alpha_n^{(0)} \Delta_n}\right)^2 . \tag{S13}$$

Evaluation of Eq. (S13) requires the coefficients for the zeroth moment, $\alpha_n^{(0)}$, first moment, $\alpha_n^{(1)}$ and the second moment, $\alpha_n^{(2)}$. Evaluating the coefficients $\alpha_n^{(2)}$ over the interval in Eq. (S10), as before, yields the results in Supplementary Fig. 1b. Again note the excellent agreement with the required result in Eq. (S12).

Since a narrow doubly-clamped beam can be represented as a one-dimensional resonator, the standard deviation and all higher order quantities are specified solely along the beam axis, *i.e.* in the *x*-direction. In this simplest case, we exclude higher families of modes, *e.g.* torsional, *etc.*

Third moment (asymmetry):

To evaluate the third moment, we require the coefficients $\alpha_n^{(3)}$ such that

$$g^{(3)}(x) = \sum_{n=1}^{N} \alpha_n^{(3)} \Phi_n^2(x) = x^3, \tag{S14}$$

The skewness, η_x, is then specified by

$$\eta_x = \left(\frac{\left(\mathrm{m}^{(0)}\right)^2}{\mathrm{m}^{(0)}\mathrm{m}^{(2)} - \left(\mathrm{m}^{(1)}\right)^2} \right)^{\frac{3}{2}} \left(\frac{\mathrm{m}^{(3)}}{\mathrm{m}^{(0)}} - 3\frac{\mathrm{m}^{(1)}\mathrm{m}^{(2)}}{\left(\mathrm{m}^{(0)}\right)^2} + 2\left(\frac{\mathrm{m}^{(1)}}{\mathrm{m}^{(0)}} \right)^3 \right), \tag{S15}$$

where, as previously defined,

$$\mathrm{m}^{(3)} = -2M \sum_{n=1}^{N} \alpha_n^{(3)} \Delta_n \ . \tag{S16}$$

Note that the formulas above for analyte position, variance and skewness are independent

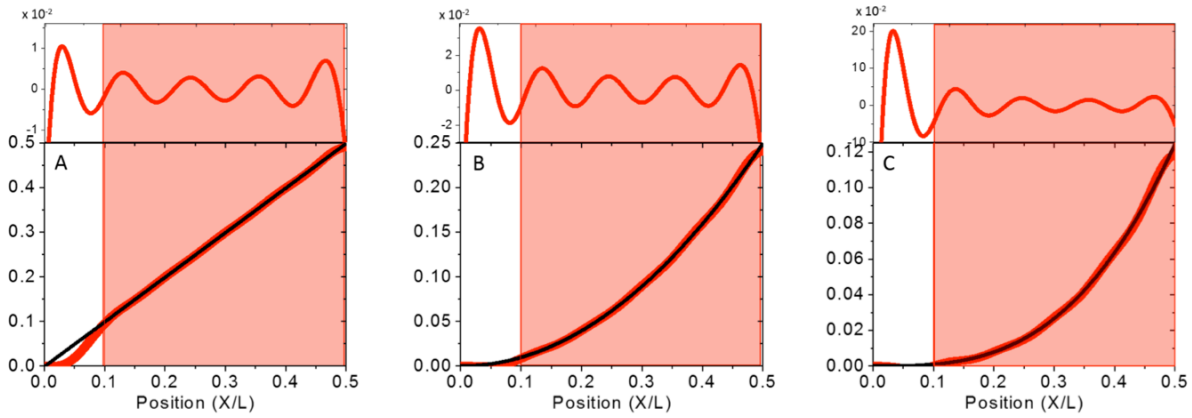

Supplementary Figure 1 | Ten-mode superposition functions to calculate the first, second and third moments. Bottom row: Red curves are the superposition function as a linear combination of the mode shapes. These are created using the coefficients to calculate the 1st, **a,** 2nd, **b**, and 3rd , **c,** moments of the mass distribution of the particle. Red shading indicates the measurement zone used for these calculations ([N / (1+N^2), ½]). The solid black curves represent the fitting functions. It is clearly seen that the superpositions well match the fitting function within the measurement zone, but depart in the region (unshaded) outside the measurement zone. Top row: the residual of the superposition curves as approximations to the fitting function.

of the device mass, *M*; again, they are specified only along the longitudinal beam axis, *x*.

The coefficients $\alpha_n^{(3)}$ required to calculate skewness are again evaluated over the interval in Eq. (S10), and corresponding results for $g^{(3)}(x) = x^3$ are given in Supplementary Fig. 1c.

3. Uniqueness of solution

The function $g^{(k)}(\mathbf{r})$ specifies the order of the moments, $\mathrm{m}^{(k)}$, in Eq. (3) (main text), and is expressed as a linear superposition over the squared magnitude of the mode shapes:

$$g^{(k)}(\mathbf{r}) = \sum_{n=1}^{N} \alpha_n^{(k)} \left|\mathbf{\Phi}_n(\mathbf{r})\right|^2 . \tag{S17}$$

Here, the unknown coefficients, $\{\alpha_n^{(k)}\}$, are determined using a least-squares analysis. We derive an explicit solution for them, which provides a condition for the uniqueness of solution.

The goal of the least-squares analysis is to determine the fit parameters, $\{\alpha_i^{(k)}\}$, such that the residual

$$\Theta^2\left(\{\alpha_i^{(k)}\}\right) \equiv \int_\Omega \left(\sum_{n=1}^{N} \alpha_n^{(k)} \left|\mathbf{\Phi}_n(\mathbf{r})\right|^2 - g_{\mathbf{exact}}^{(k)}(\mathbf{r}) \right)^2 dV , \tag{S18}$$

is minimized, where $g_{\mathrm{exact}}^{(k)}(\mathbf{r})$ is the exact function to be approximated by Eq. (S17). The coefficients are specified by the stationary condition:

$$\frac{\partial \Theta^2}{\partial \alpha_i^{(k)}} = 0 . \tag{S19}$$

From Eqs. (S18) and (S19) we obtain

$$T_{mn}\alpha_n^{(k)} = b_m, \tag{S20}$$

where

$$T_{mn} = \int_\Omega \left|\mathbf{\Phi}_m(\mathbf{r})\right|^2 \left|\mathbf{\Phi}_n(\mathbf{r})\right|^2 dV \quad , \tag{S21}$$

$$b_m = \int_\Omega g_{\mathbf{exact}}^{(k)}(\mathbf{r}) \left|\mathbf{\Phi}_m(\mathbf{r})\right|^2 dV \ . \tag{S22}$$

Thus, provided that the inverse, T_{mn}^{-1}, exists, the unique solution to the fit parameters, $\{\alpha_i^{(k)}\}$, is

$$\alpha_n^{(k)} = T_{mn}^{-1} b_m . \tag{S23}$$

The condition of uniqueness of solution thus reduces to establishing that the matrix T_{mn} is non-singular.

While a general proof establishing the singular or non-singular nature of T_{mn} is difficult to obtain for an arbitrary device, it can be determined straightforwardly for a specific device once the modes $\mathbf{\Phi}_m(\mathbf{r})$ have been evaluated. For the doubly-clamped beam we consider in the main text, the matrix T_{mn} is non-singular; therefore, the least-squares analysis provides a unique solution to the fit parameter $\{\alpha_i^{(k)}\}$.

4. Uncertainty in least squares analysis

Here we show that the RMS error (square root of the residual), Θ, in Eq. (S18), decreases polynomially as the measurement zone is reduced, and exhibits a super-exponential decrease as the number of modes, *N*, is increased. As in the main text, we consider a (one-dimensional)

doubly-clamped beam. The particle is centered at the position, x_0, and the spatial extent of the measurement zone is $2x'$, i.e., the measurement zone is $x_0 - x' \le x \le x_0 + x'$.

For this device and measurement zone, Eq. (S18) becomes

$$\Theta^2\left(\left\{\alpha_i^{(k)}\right\}\right) \equiv \int_{x_0-x'}^{x_0+x'} \left[g^{(k)}(x) - g_{\mathbf{exact}}^{(k)}(x) \right]^2 dx, \tag{S24}$$

where

$$g^{(k)}(x) = \sum_{n=1}^{N} \alpha_n^{(k)} \Phi_n^2(x) . \tag{S25}$$

Throughout we assume $x' << 1$, and examine the effect of reducing the measurement zone size. Accordingly, we approximate both $g^{(k)}(x)$ and $g_{\mathrm{exact}}^{(k)}(x)$ by their Taylor expansions around x_0,

$$g_{\mathbf{exact}}^{(k)}(x) = \sum_{m=0}^{\infty} \frac{(x-x_0)^m}{m!} \left. \frac{\partial^m g_{\mathbf{exact}}^{(k)}}{\partial x^m} \right|_{x=x_0} , \tag{S26}$$

$$g^{(k)}(x) = \sum_{n=1}^{N} \alpha_n^{(k)} \sum_{m-0}^{\infty} \frac{(x-x_0)^m}{m!} \left. \frac{\partial^m \Phi_n^2}{\partial x^m} \right|_{x=x_0} . \tag{S27}$$

Substituting the Taylor expansions, Eqs.(S26) and (S27) into Eq.(S24) gives

$$\Theta^2 = 2 \sum_{m=0}^{\infty} \frac{(x')^{2m+1}}{(2m+1)(m!)^2} \left(\left. \frac{\partial^m g_{\mathbf{exact}}^{(k)}}{\partial x^m} \right|_{x=x_0} - \sum_{n=1}^{N} \alpha_n^{(k)} \left. \frac{\partial^m \Phi_n^2}{\partial x^m} \right|_{x=x_0} \right)^2 . \tag{S28}$$

Since Eq. (S28) is an asymptotic (power series) expansion in x', the coefficients $\alpha_n^{(k)}$ that minimize the residual are specified by the zeros of each term in the sum over *m*, *i.e.*

$$\left.\frac{\partial^m g_{\mathbf{exact}}^{(k)}}{\partial x^m}\right|_{x=x_0} - \sum_{n=1}^{N} \alpha_n^{(k)} \left.\frac{\partial^m \Phi_n^2}{\partial x^m}\right|_{x=x_0} = 0 \ . \tag{S29}$$

Importantly, a finite number of coefficients $\alpha_n^{(k)}$ exist in Eq. (S29); for $n = 1, 2, ..., N$. Thus, to ensure a unique solution, Eq. (S29) must contain *N* independent equations, $m = 0, 1, 2, ..., N-1$. Substituting Eq. (S29) into Eq. (S28) thus yields the dominant term:

$$\Theta^2 = \frac{2\left(x'\right)^{2N+1}}{\left(2N+1\right)\left(N!\right)^2}\left(\left.\frac{\partial^N g_{\mathbf{exact}}^{(k)}}{\partial x^N}\right|_{x=x_0} - \sum_{n=1}^{N} \alpha_n^{(k)} \left.\frac{\partial^N \Phi_n^2}{\partial x^N}\right|_{x=x_0} \right)^2 + O\left(\left[\left(x'\right)^{2N+3}\right]\right). \tag{S30}$$

As such, we find that for large *N* the leading order behavior of the square root of the residual is

$$\Theta^2 = \frac{2\left(x'\right)^{2N+1}}{\left(2N+1\right)\left(N!\right)^2}\left(\left.\frac{\partial^N g_{\mathbf{exact}}^{(k)}}{\partial x^N}\right|_{x=x_0} - \sum_{n=1}^{N} \alpha_n^{(k)} \left.\frac{\partial^N \Phi_n^2}{\partial x^N}\right|_{x=x_0} \right)^2 + O\left(\left[\left(x'\right)^{2N+3}\right]\right), \tag{S31}$$

where

$$f^{(N)}\left(x_0\right) = \left.\frac{\partial^N g_{\mathbf{exact}}^{(k)}}{\partial x^N}\right|_{x=x_0} - \sum_{n=1}^{N} \alpha_n^{(k)} \left.\frac{\partial^N \Phi_n^2}{\partial x^N}\right|_{x=x_0} \ . \tag{S32}$$

Equation (S31) is the required result; it shows that the RMS error (square root of residual) exhibits super-exponential convergence in the number of modes, *N*, and polynomial convergence with respect to the measurement zone size, $2x'$. The function $f^{(N)}$, converges with increasing *N* as the superposition of mode shapes (and the N^{th} derivatives thereof) better approximate $g_{exact}^{(k)}$.

5. Minimum number of modes required for inertial imaging with a doubly-clamped beam

We calculate the number of modes, *N*, required to determine the mass, position, standard deviation and skewness of an adsorbate, in the limit where the adsorbate and measurement zone size vanish. Recall that the adsorbate must lie within the measurement zone. Therefore, this calculation gives the minimum number of modes required to measure the properties of infinitesimally small adsorbates.

The measurement zone is centered at $x = x_0$, and spans the domain $x_0 - x' \le x \le x_0 + x'$. Shrinking the measurement zone to zero thus formally corresponds to taking the asymptotic limit, $x' \to 0$. To obtain an exact measurement in this asymptotic limit, $g^{(k)}(x)$ must exactly represent $g^{(k)}_{\text{exact}}(x)$. We formally expand $g^{(k)}(x)$ in its Taylor series about $x = x_0$:

$$g^{(k)}(x) = \sum_{n=1}^{M} \left.\frac{\partial g^{(k)}}{\partial x}\right|_{x=x_0} \frac{(x-x_0)^n}{n!} + O\left([x-x_0]^{M+1}\right) . \tag{S33}$$

5.1 Mass (zeroth moment)

We first consider the measurement of analyte mass, for which $g^{(0)}_{\text{exact}}(x) = 1$. If we use only one mode, $N = 1$, then equating the leading order term in Eq. (S33) to $g^{(0)}_{\text{exact}}(x)$ gives

$$1 = \alpha_1^{(0)} \Phi_1^2(x_0) + O(x - x_0) , \tag{S34}$$

which has the solution, $\alpha_1^{(0)} = 1/\Phi_1^2(x_0)$. Thus, one mode is sufficient to represent the function $g^{(0)}_{\text{exact}}(x) = 1$ in the measurement zone. In the limit $x' \to 0$ this is asymptotically exact since all

higher order terms in the Taylor expansion (Eq. (S33)) vanish. Therefore, as the size of the adsorbate vanishes, *i.e.* as the particle becomes point-like, only one mode ($N = 1$) is required to measure its mass.

Using more than one mode, $N > 1$, enables higher order terms in the Taylor expansion, Eq. (S33), to be set to zero. However, their inclusion is inconsequential to the accuracy of the measured mass, since these terms vanish in the limit, $x' \to 0$; hence, use of more than one mode simply rearranges the distribution of the coefficients $\alpha_n^{(k)}$, with no effect on the measured mass.

5.2 Centre-of-mass position (first moment)

In this case, the required function is $g_{\text{exact}}^{(1)}(x) = x$. As before, we first assume use of only one mode, *i.e.*, $N = 1$, and equate the leading-order term in Eq. (S33) to $g_{\text{exact}}^{(1)}(x)$ – this gives $x = \alpha_1^{(1)}\Phi_1^2(x_0) + O(x - x_0)$, which has no solution. Thus, frequency jumps from a single mode alone cannot provide analyte position measurements.

However, using two modes ($N = 2$) gives:

$$x = \alpha_1^{(1)}\Phi_1^2(x_0) + \alpha_2^{(1)}\Phi_2^2(x_0) + (x - x_0)\left\{\alpha_1^{(1)}\Phi_1(x_0)\frac{\partial\Phi_1(x_0)}{\partial x} + \alpha_2^{(1)}\Phi_2(x_0)\frac{\partial\Phi_2(x_0)}{\partial x}\right\} + O(x - x_0)^2 . \qquad \text{(S35)}$$

This has a unique solution that can be obtained upon equating powers of x. This yields two simultaneous equations for the unknown coefficients, $\alpha_1^{(1)}$, $\alpha_2^{(1)}$. Consequently, use of two modes is sufficient to represent the function $g_{\text{exact}}^{(1)}(x) = x$, in the limit $x' \to 0$. Two modes ($N = 2$), therefore, allows for exact determination of particle position, as the adsorbate size vanishes.

As in the case of mass measurements (zeroth moment), use of more modes ($N > 2$) enables higher order terms in the Taylor expansion to be set to zero. Since these terms vanish as $x' \to 0$, we find that use of only 2 modes enables the exact position to be determined. Use of more than two modes does not affect position determination in this limit.

5.3 Standard deviation, skewness, and higher moments

A similar analysis can be applied to evaluation of the higher moments of the mass density distribution, e.g., $g^{(2)}(x) \approx x^2$, $g^{(3)}(x) \approx x^3$, etc. These moments enable measurement of the standard deviation, skewness, and higher asymmetries of the adsorbate's density distribution, *i.e.*, its size and shape. It can be easily shown, in a manner analogous to that performed for the mass and position (above), that the number of modes required to exactly measure the n^{th} moment is $N = n + 1$, in the limit of an adsorbate of infinitesimal size. As above, use of additional modes has no effect on the accuracy of the measured moments, in this limit.

6. Initial measurement zone for a doubly-clamped beam

The mass responsivity of a doubly-clamped beam vanishes at its clamping ends. Accordingly, adsorption events very close to these regions must be excluded as they will provide frequency jumps with poor signal-to-noise ratios. Figure 1c of the main text illustrates that $g^{(0)}(x)$ converges to unity over an increasingly wider region, as additional modes are included. This region is termed the "measurement zone". We define the spatial extent of this region by an accuracy criterion, prescribed below.

The spatial extent over which calculated values for the adsorbed mass, *m*, converge depends upon the number of modes employed; this coincides with the measurement zone. For *N* modes, the measurement zone is defined to be $\Omega_l^{(N)}$ and spans the region $x \in [\frac{1}{2} - \Delta x_N, \frac{1}{2} + \Delta x_N]$; regions of length Δx_N at the clamped ends are excluded. Our aim is to determine Δx_N such that measured accuracy of the adsorbate, in the measurement zone, is specified.

Accuracy Criterion: The length Δx_N is calculated using the following criterion: The function $g^{(0)}(x)$ is identical to unity in the measurement zone, $\Omega_l^{(N)}$, to within a specified tolerance δ, i.e.,

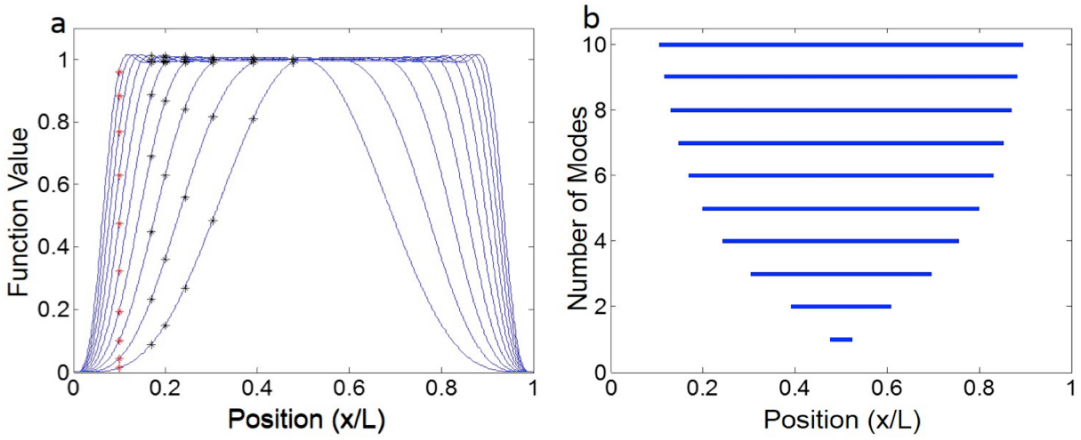

Supplementary Figure 2 | Dependence of the initial measurement zone on the number of modes employed. a, One to ten modes are superposed to yield the function $g^{(0)}(x) = 1$. Black dots indicate the relative value of the measured mass of a particle at a given position, for inertial imaging calculations for mass using different numbers of modes. The red dots show the values for a particle landing outside the ten-mode measurement zone. **b,** The extent of the measurement zone for calculations involving different numbers of modes (from one to ten).

$$g^{(0)}(x) - 1 \leq \delta \tag{S36}$$

for all positions x within $\Omega_l^{(N)}$. This guarantees that the measured mass is determined to within the same accuracy, in the measurement zone. We choose the nominal value, $\delta = 0.01$, corresponding to 1% tolerance.

For N = 1, the measurement zone is in the immediate vicinity of $x = 1/2$. However, a small deviation from this position, for example at $x = 0.4$, leads to a significant deterioration in accuracy. Increasing the distance from the beam center enhances the error monotonically; see Supplementary Fig. 2a.

The situation improves for N = 2, where the measurement zone size increases markedly. The measured mass of the particle at position, $x = 0.4$, is now in good agreement with the true value, as illustrated in Supplementary Fig. 2a. Nonetheless, as the adsorption position moves closer to the clamped ends, the mass error again increases.

For $N \geq 2$, the size of the measurement zone increases monotonically with N and adsorption positions closer to the clamped ends can yield good mass accuracy. We thus observe that increasing the number of modes extends the spatial extent of the measurement zone.

This measurement zone specification Eq. (S10) is well approximated by:

$$\frac{N}{1+N^2} \leq x \leq 1 - \frac{N}{1+N^2} \ ; \tag{S37}$$

we use this criterion in all of the calculations reported in the main text.

Since the mode shapes vanish at the clamped ends, adsorption in the immediate vicinity of the clamps cannot provide good mass accuracy, regardless of the number of modes used. This is reflected in Eq. (S37), which excludes the clamped ends for any finite number of modes, N.

Supplementary Fig. 2b illustrates the measurement zones (as specified by the above accuracy criterion) for N = 1 to 10. For analytes adsorbed within these zones (pictured), mass determination with good accuracy is possible. As the number of modes is increased, the measurement zone expands, allowing larger useful capture cross-sections for the device.

From the considerations above, we now formulate an operational method for quickly determining whether a randomly placed adsorbate falls within the measurement zone $\Omega_l^{(N)}$. Importantly, mass error decreases monotonically with increasing N for adsorption outside the measurement zone, but is invariant (to within δ = 1%) within the measurement zone for n= {1,2}, {1,2,3},….. {1,N}; see Supplementary Fig. 2a. Thus, by measuring the adsorbate mass using an increasing number of modes, from 1 up to N modes, the presence of the adsorbate within the measurement zone for N modes can be readily established. The precise location of the adsorbate need not be determined for this purpose.

The chosen tolerance level of δ = 1% approximately matches the empirical measurement zone, Eq. (S37). Reducing this tolerance level leads to a smaller measurement zone size, whereas increasing δ sacrifices measurement accuracy for spatial extent. As will be shown in the next section, adaptive fitting can dramatically improve the accuracy level below this initial tolerance level, δ.

7. Demonstration of adaptive fitting for a doubly-clamped beam

As discussed in Section 4, a reduction in measurement zone size decreases the residual in the least-squares analysis. Importantly, this residual is directly related to measurement accuracy. We can therefore systematically reduce the measurement zone size using adaptive fitting, as described below, to systematically improve the accuracy of all moments. This in turn enhances the accuracy of adsorbate attributes determined from them, namely: mass, mean (centre-of-mass

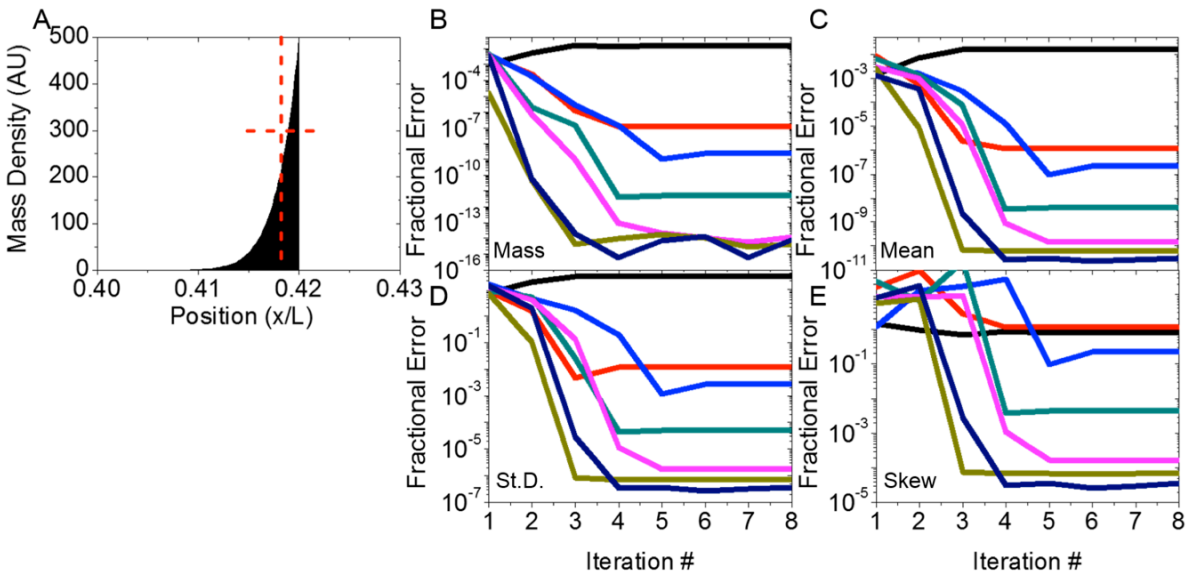

Supplementary Figure 3 | Simulated adaptive fitting results for a highly skewed particle. A discrete analyte with skew is placed at a specific position along the beam. **a,** The particle's mass density distribution. Vertical (horizontal) dotted red line indicates the mean (twice the standard deviation). **b-e,** The fractional errors of the moments of the mass distribution function for the particle, calculated by inertial imaging theory, for the mass (0^{th} moment), centre-of-mass position (mean, 1^{st}), particle size, i.e., standard deviation (SD.; 2^{nd}), and particle asymmetry, i.e., skewness (3^{rd}), respectively. Colors indicate the highest number of modes used with [black, red, blue, cyan, magenta, yellow, navy] representing [2, 3, 4, 5, 6, 8, 10] modes, respectively.

position), standard deviation (particle size), and skewness (first asymmetry moment).

Adaptive fitting: The measurement zone in this (iterative) adaptive fitting procedure is chosen to be

$$\langle x \rangle - 2\sigma_x \leq x \leq \langle x \rangle + 2\sigma_x \tag{S38}$$

where $\langle x \rangle$ is the measured mean position of the adsorbate, and σ_x is its measured standard deviation, both evaluated using the previously chosen measurement zone.

Initially, the measurement zone size is set to its maximum value, using Eq. (S37). The position and standard deviation of the adsorbate are then determined. These values are substituted into Eq. (S38), which defines a new (reduced) measurement zone, from which new estimates of the moments are determined. This procedure is repeated until convergence is achieved. Since a reduction in measurement zone size improves the accuracy of measurements (see Section 4), this procedure enables maximum accuracy to be achieved.

Results of this procedure are given in Supplementary Figures 3b-e, where it is observed that the fractional errors plateau after about 3-5 iterations of adaptive fitting. Note that a dramatic reduction in measurement error is achieved using only a few iterations, with fractional errors decreasing by many orders of magnitude. As expected, the error decreases as the number of modes used increases; this feature is also discussed in Supplementary Information, Section 4.

8. Inertial imaging validation using finite element simulations

We present finite element method (FEM) simulations of the response of a device to a test particle. Two different types of simulations were performed: simulations based on Mindlin Plate theory and simulations in full 3D. The results of inertial imaging correctly predicts the spatial properties of the analytes in both types of simulations.

FEM simulations with Mindlin thick plate theory (COMSOL) were performed to facilitate accurate simulation of higher order moments, such as kurtosis; this was limited only by available computational resources. The analyte is modeled as a small rectangular addendum to a doubly clamped beam – with specific mass, position, density, stiffness, and shape shown in Supplementary Fig. 4a. For illustrative purposes the particle is defined to be much smaller than the wavelength of the highest mechanical mode employed in the expansions for the moments, $\{\mathrm{m}^{(k)}\}$. The test particle's mass distribution is asymmetric and has a step-like density profile (Supplementary Fig. 4b); this gives it high spatial Fourier components. Particle-induced frequency shifts for the first five out-of-plane displacement modes are calculated and these are, in turn, used to calculate the first five moments by inertial imaging theory. From these moments we deduce particle mass, position, size, skewness and kurtosis. As seen in Supplementary Fig. 4c, moments deduced from inertial imaging theory are accurate.

a

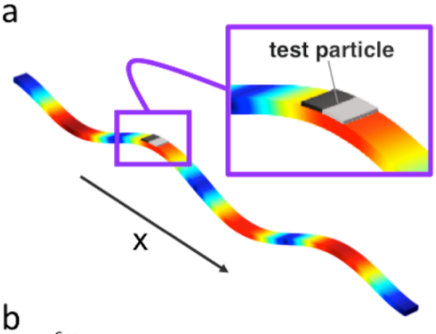

b

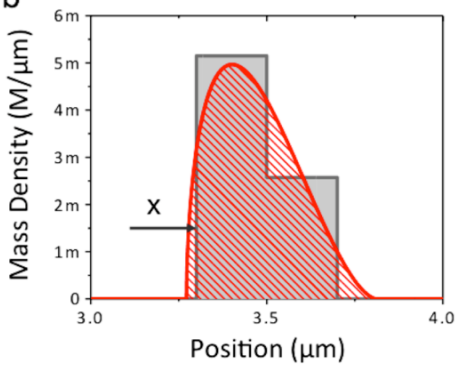

c

Simulations - Mindlin Theory

Parameter	Simulated Value	Calculated Value
Mass (x 10^{-3})	1.545	1.540 ± 0.005
Mean Position (nm)	3,467	3,467 ± 2.5
Std. Deviation (nm)	111	113 ± 4.8
Skewness	0.439	0.424 ± 0.075
Kurtosis	2.12	2.41 ± 0.29

d

Simulations – Full 3D

Placement Position (μm)	Calculated Position (μm)	Mass (x10^{-3}M)	Std. Dev.(nm)
2.6	2.604	2.830	118
3.4	3.410	2.829	115
4.0	4.011	2.835	116
Actual values:		2.861	115

Supplementary Figure 4 | FEM Simulations of inertial imaging. **a,** A rectangular test particle (gray) is place at a random position along a doubly-clamped beam. A snapshot of displacement for the fourth out-of-plane flexural mode of the beam is shown. Colors represent displacement magnitude. The physical characteristics of the beam are the same as those in [1]. **b,** The simulated density profile of the test particle in the *x*-direction (gray) revealing a step-wise distribution. The spatial moments derived using inertial imaging are used to recreate an approximation of the original distribution using Pearson's method (red). The frequency shifts in the first five out-of-plane displacement beam modes were used. **c,** The simulated and calculated values of the first five spatial moments of the particle using the same frequency shifts utilized in (b). The 2 g/cm^3 particle density used, although somewhat higher than that of typical biological analytes, provides a clear illustration. **d,** Simulation results for a full 3D solution are shown. In this case, the analyte is a 400 x 100 x 10 nm (*Lwt*) particle firmly attached to a 10,000 x 300 x 100 nm (*Lwt*) doubly-clamped Si nanomechanical resonator. Densities for the particle and beam are 5.00 and 2.33 g/cm^3, respectively. The particle has a Young's Modulus of 10 MPa. The first four beam modes are used to calculate the adsorption-induced frequency shifts for these modes – this is performed for several positions shown in the table. An Allan deviation of ~5×10^{-5} is assumed for all modes used in the simulation. As displayed in the table, the inertially-imaged values for particle mass, position, and size are in excellent agreement (less than a few percent) with actual particle

It is possible to reconstruct the test particle's inertial image from these deduced moments by employing a variety of different techniques [3-7]. To provide a concrete demonstration, we employ the Pearson distribution method [8]. In Supplementary Fig. 4b we compare the reconstructed image with the original, simulated density profile. As shown, the reconstructed image is in good agreement with the abrupt original mass distribution; this shows good fidelity considering that only five moments of the distribution were used. FEM simulations for different particle positions were conducted to further validate the inertial imaging method. Discretization error present in FEM is the primary source of uncertainty in these simulations (convergence information is provided in the next section).

The mesh used in these simulations was systematically refined until a convergence of 2×10^{-5} (fractional difference in eigenfrequencies for a twofold increase in mesh size) was achieved. The final mesh used in the simulation contains 1.6 million elements. In the simulations, three different placement positions were used. In each position, the particle was simulated both for positive and negative skew configurations. The results of these simulations yield similar performance in estimating the physical parameters of the particle and these values are used to calculate the error statistics reported in Supplementary Fig. 4c. The observed error in Supplementary Fig. 4c is approximately correlated with increasing statistical order, i.e., mass, position, SD, skewness, kurtosis, and is due to an accumulation of FE discretization error, as expected.

The results for full 3D simulations are shown in Supplementary Fig. 4d. For these simulations, a symmetric particle is located at different places among the beam. The first three moments of the particle (mass, position and standard deviation) are calculated and compared

with the simulated values. To within the estimated uncertainty, these simulations agreed with the Mindlin simulations of the device. However, 3D simulations were computationally expensive and did not allow for evaluation of the kurtosis with sufficient convergence, hence motivating the use of Mindlin plate theory. The numerical accuracy of the 3D simulations for the determination of the fractional frequencies is found to be $\sim 5\times10^{-5}$. This finite numerical accuracy plays a somewhat similar role to frequency noise in real experiments; in this way uncertainty estimates for different moments can be obtained. As seen in Supplementary Fig. 4d (for full 3D simulations), values measured using inertial imaging theory are all well within expected uncertainties of the different modes as determined by the numerical accuracy levels.

9. Convergence of FEM Simulations

For Mindlin plate theory, the same mesh was used for loaded and unloaded beams; this was systematically refined until convergence was achieved. For the 3D simulations, however, since different meshes are obviously required for loaded and unloaded cases, an alternate procedure was used. The 3D mesh was systematically refined for the loaded and unloaded cases independently, the resonance frequencies extracted in each case, and convergence of the fractional frequency shift monitored until the required convergence was achieved. Frequency shifts for the first four modes were obtained by FEM analysis. These were substituted into inertial imaging theory to obtain results for mass, position, and variance of the test particle. As seen in Supplementary Fig. 5, mesh refinement not only results in convergence towards the expected values, but also reduces the scatter in values obtained at different positions along the beam. Note that the deduced mass values converge to a slightly different value than the exact

result. This reflects a small (~1%) and expected systematic error between Euler-Bernoulli beam theory and the full 3D FEM. These results thus validate the robustness of the inertial imaging theory, and the accuracy of the FEM results we present. Again, similar results were obtained for Mindlin plate theory (not shown).

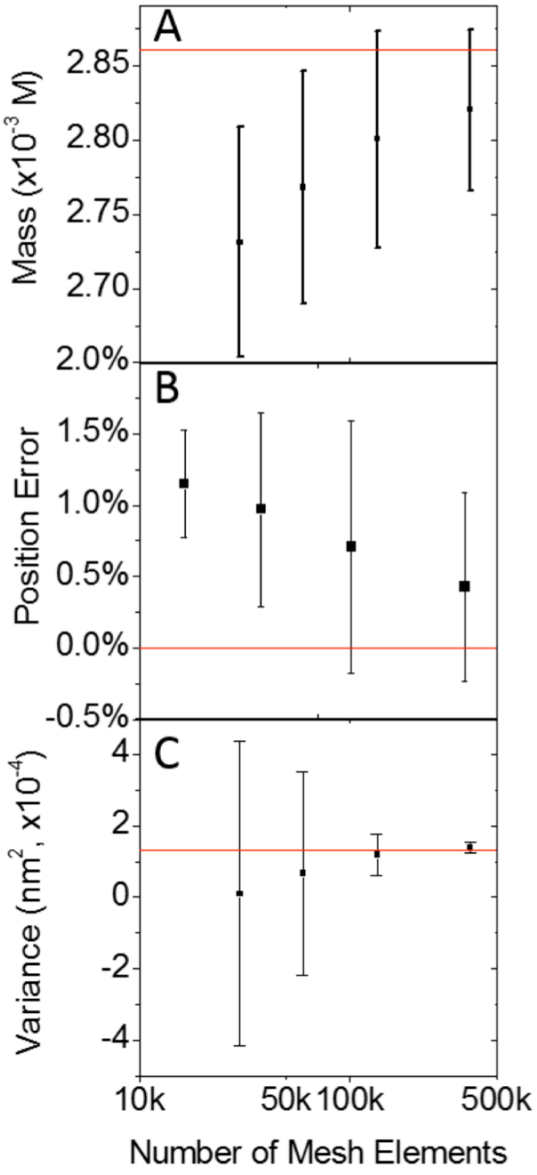

Supplementary Figure 5 | Convergence of FEM simulations for estimation of particle size.

a, The calculated mass averaged over 8 different beam positions as a function of number of mesh elements used in the FEM simulation. **b,** The error in the position calculation averaged over all 8 positions as fractional percent of the simulated centre-of-mass of the particle. **c,** Same as in (a), but now for the variance of the particle distribution. In all plots, the error bars (rendered at 2-sigma level) are calculated by the statistics of size estimates at 8 different places along the beam. The red lines show the expected value of the measured quantity for the simulated particle.

10. Effect of frequency noise on adsorbate size measurement using a doubly-clamped beam

To measure the adsorbate's size, the zeroth, first, and second moments must be considered, and the corresponding coefficients $\alpha_n^{(0)}, \alpha_n^{(1)}, \alpha_n^{(2)}$ evaluated. The standard deviation of the adsorbate's spatial density distribution can then be measured using

$$\sigma_x^2 \approx \frac{\mathrm{m}^{(2)}}{\mathrm{m}^{(0)}} - \left(\frac{\mathrm{m}^{(1)}}{\mathrm{m}^{(0)}} \right)^2 , \tag{S39}$$

where

$$\mathrm{m}^{(k)} = -2M \sum_{n=1}^{N} \alpha_n^{(k)} \Delta_n \ , \tag{S40}$$

and the coefficients $\alpha_n^{(k)}$ are solved using:

$$g^{(k)}(x) = \sum_{n=1}^{N} \alpha_n^{(k)} \Phi_n^2(x) = x^k \tag{S41}$$

over a specified measurement zone.

Since the uncertainty in size dominates the uncertainty in mass and position – size is derived using calculated mass and position values (see Eq. (S39)) – we can directly calculate the statistical uncertainty, Γ, due to frequency noise. For cases where the error in the lower order moments is significant, the uncertainty in higher order moments will reflect this error in lower order moments. This dependence can be calculated through standard error propagation procedures. We characterize the relative strength of frequency fluctuations in each mode, *n*, by their Allan deviations $\sigma_{A,n}$. In general, these are different for each mode, *n*.

$$\Gamma\left(\left\{\sigma_{A,n}\right\}_N\right) \approx \sqrt{\frac{4\sum_{n=1}^{N}\left(\alpha_n^{(2)}\sigma_{A,n}\right)^2}{\left(\frac{m}{M}\right)^2}} \quad . \tag{S42}$$

The adsorbate and total beam masses are m and M, respectively. Γ is then the statistical uncertainty in the standard deviation of the adsorbate's distribution. Heavier adsorbates, relative to the beam, are thus easier to image as they register a larger frequency response compared to the frequency noise. As the adsorbate's size is reduced, frequency fluctuations will dominate the residual error illustrated in Figures 1 and 2 of the main text. Thus, the adsorbate-size resolution of a given system is fully determined by Eq. (S42). This equation indicates that use of additional modes is helpful only if those modes do not involve too much additional frequency noise.

11. Liquid droplet array measurements

Liquid droplets were deposited on a tipless, Bruker CLFC-NOBO single-crystal Si reference cantilever (Lever C), with nominal dimensions: length = 397μm, width = 29 μm, and thickness = 2μm. This yields a nominal force constant ~0.157 N/m and a typical fundamental resonance frequency of ~18kHz. Dip-pen lithographic definition of the droplets was carried out using a separate AFM tip coated in a liquid adhesive (Norland Optical Adhesive 65 obtained from Norland Products) that was manipulated by an Asylum Research MFP-3D AFM as described elsewhere [9,10]. Array droplets were deposited in pairs, in the order of left to right, beginning near the distal (free) end of the cantilever. Power spectral density measurements of the cantilever's thermomechanical noise were performed at ambient temperature (22 C) and pressure (in air), before and after droplet deposition. The nominal viscosity of the uncured liquid

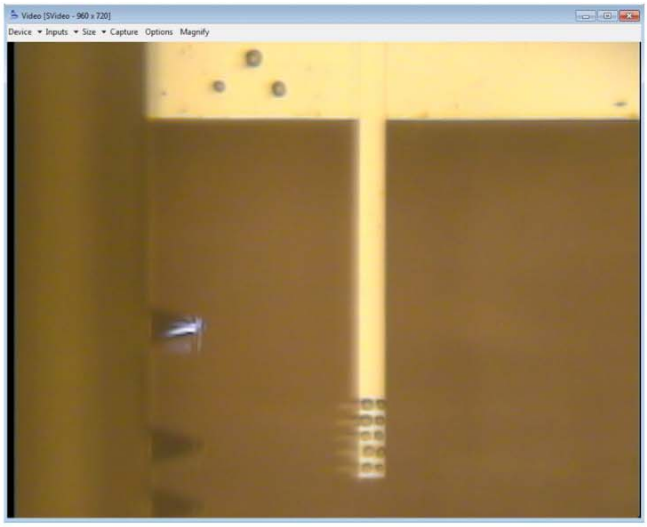

Supplementary Figure 6 | Dip-pen lithography setup. Screen capture of a tipless Bruker CLFC-NOBO single-crystal Si reference cantilever with a deposited droplet array (lower center). The deposition cantilever (visible at the left) used for dip-pen lithographic deposition of the droplets, is manipulated using an Asylum Research MFP3D.

adhesive is stated to be 1200 cP. A negligible change in our measured data (below measurement uncertainty) was measured after UV curing, *i.e.* solidifying, the droplets per manufacturer's instructions. We also performed measurements to assess possible effects due to evaporation of volatiles in the adhesive. Again, no changes in results were observed, *i.e.* no detectable frequency shifts for uncured droplets even several days after their deposition on a cantilever. (The manufacturer (Norland) specifies the adhesive to contain minimal volatile components.)

Below, the measured resonant frequencies before and after droplet deposition are given in Supplementary Table 1. We present their relative uncertainties in Supplementary Table 2; these are determined using the protocol described in Ref. [11].

Supplementary Table 1. Measured resonant frequencies of microcantilever, with and without droplet arrays.

Mode	Resonant frequency (Hz)$\times 10^{-5}$						
	Unloaded	One row	Two rows	Three rows	Four rows	Five rows	Asymmetric
1	0.17883	0.17777	0.17680	0.17610	0.17493	0.17406	0.17639
2	1.12465	1.11919	1.11596	1.11482	1.11412	1.11413	1.11629
3	3.15158	3.13857	3.13489	3.13469	3.13344	3.12790	3.13271
4	6.17728	6.15718	6.15523	6.15371	6.13598	6.11124	6.13995

Supplementary Table 2. Relative uncertainty (two standard errors) in resonant frequencies of microcantilever, with and without droplet arrays.

Mode	Relative uncertainty (2SE) in Resonant frequency						
	Unloaded	One row	Two rows	Three rows	Four rows	Five rows	Asymmetric
1	8.16E-05	9.48E-05	9.36E-05	9.31E-05	9.39E-05	9.38E-05	9.21E-05
2	1.97E-05	2.22E-05	2.23E-05	2.21E-05	2.32E-05	2.22E-05	2.21E-05
3	1.16E-05	1.24E-05	1.28E-05	1.23E-05	1.44E-05	1.23E-05	1.25E-05
4	1.09E-05	1.06E-05	1.12E-05	1.05E-05	1.45E-05	1.07E-05	1.12E-05

11. Inertial Imaging of skewed droplet array

In Supplementary Fig. 7 , we present the inertial imaging results obtained for the droplet array with finite skewness. The optical image of this sample was provided as the rightmost image in Fig. 4a; it is also replicated in the image below.

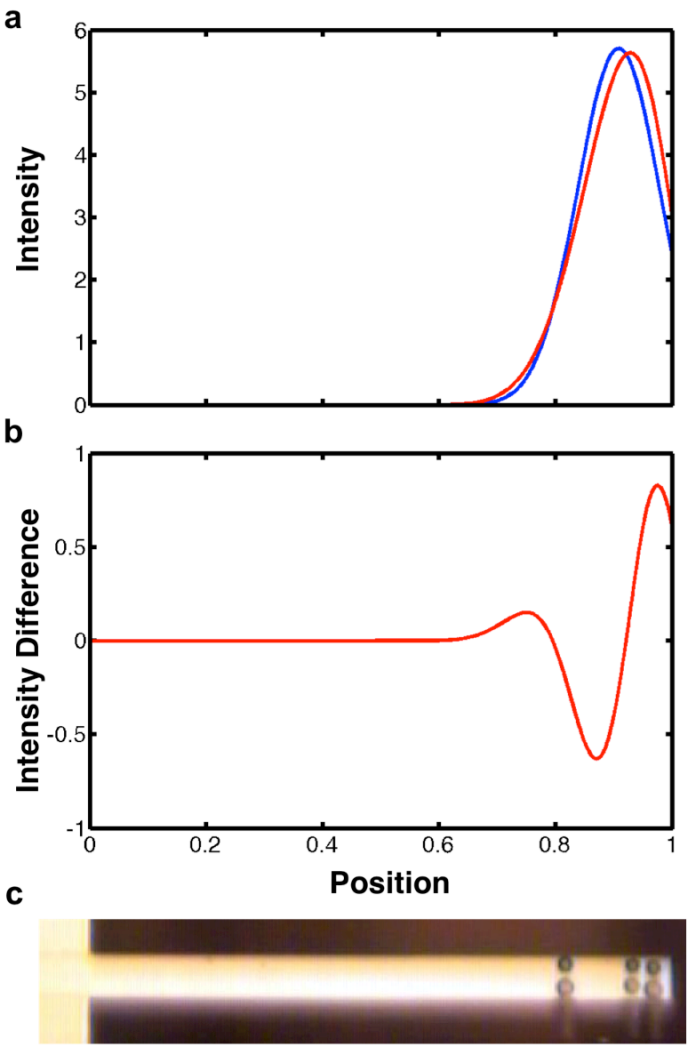

Supplementary Figure 7 | Inertial Imaging of skewed droplet array: The distribution functions obtained for the droplet array with asymmetric distribution. **a.** The reconstructed distribution functions for the case with zero skewness (blue) and with the skewness value calculated through the inertial imaging (red). **b.** The difference between the skewed and unskewed distributions. The maxima of the graph overlaps with the position of droplets, whereas the minimum region overlaps with the gap between the droplets. **c.** The image of the droplet arrays analyzed.

REFERENCES

1. Hanay, M.S., et al., *Single-protein nanomechanical mass spectrometry in real time.* Nature Nanotechnology, 2012. 7(9): p. 602-608.

2. Naik, A.K., et al., *Towards single-molecule nanomechanical mass spectrometry.* Nature Nanotechnology, 2009. 4(7): p. 445-450.

3. Hausdorff, F., *Moment problems for a infinite interval.* Mathematische Zeitschrift, 1923. **16**, 220.

4. Athanassoulis, G.A. and P.N. Gavriliadis, *The truncated Hausdorff moment problem solved by using kernel density functions.* Probabilistic Engineering Mechanics, 2002. **17**(3): p. 273-291.

5. Mead, L.R. and N. Papanicolaou, *Maximum-Entropy in the Problem of Moments.* Journal of Mathematical Physics, 1984. **25**(8): p. 2404-2417.

6. Ngoc, T.M.P., *A statistical minimax approach to the Hausdorff moment problem.* Inverse Problems, 2008. **24**(4).

7. Wu, X.M., *Calculation of maximum entropy densities with application to income distribution.* Journal of Econometrics, 2003. **115**(2): p. 347-354.

8. Au-Yeung, S.W., *Finding probability distributions from moments.* Master's Thesis, Imperial College, London, 2003.

9. O'Connell, C. D., Higgins, M. J., Marusic, D., Moulton, S. E. & Wallace, G. G. *Liquid ink deposition from an atomic force microscope tip: deposition monitoring and control of feature size.* Langmuir **30**, 2712–21 (2014).

10. O'Connell, C. D., Higgins, M. J., Sullivan, R. P., Moulton, S. E. & Wallace, G. G. *Ink-on-Probe Hydrodynamics in Atomic Force Microscope Deposition of Liquid Inks.* Small **1**, 12 (2014).

11. Sader, J. E., Yousef, M. & Friend, J. R., *Uncertainty in least-squares fits to the thermal noise spectra of nanomechanical resonators with applications to the atomic force microscope*, Review of Scientific Instruments, **85**, 025104 (2014).